



# Depth encoding PET detectors using single layer crystal array with different reflector arrangements along depths

Binqing Zhao, Zhonghua Kuang, Mingdao Sun, Chunhui Zhang, Xiaohui Wang, Ziru Sang, Qian Yang, San Wu, Juan Gao, Ning Ren, Xianming Zhang, Zhanli Hu, Junwei Du, Yongfeng Yang\*

Lauterbur Research Center for Biomedical Imaging, Shenzhen Institutes of Advanced Technology, Chinese Academy of Sciences, Shenzhen 518055, China

## ARTICLE INFO

### Keywords:

Depth encoding PET detectors  
Single layer crystal array  
Single-ended readout  
Depth of interaction

## ABSTRACT

Depth encoding detectors are preferred for PET scanners with a small ring diameter and a long axial field of view. In this work, novel depth encoding detectors using different inter-crystal reflector arrangements along the depth of single layer crystal arrays are proposed and their performance is evaluated. As compared to the previous four-layer detector with different reflector arrangements, the detectors proposed in this work are expected to improve the energy and timing resolution of the detectors.  $4 \times 4$  LYSO arrays with a crystal size of  $3 \times 3 \times 20$  mm<sup>3</sup> and  $6 \times 6$  LYSO arrays with a crystal size of  $2 \times 2 \times 20$  mm<sup>3</sup> are fabricated using two and four reflector arrangements along the crystal's depth. The LYSO arrays are single-ended read out by  $4 \times 4$  SiPM arrays with a pixel size of  $3 \times 3$  mm<sup>2</sup>. The first and second half of the crystals are clearly resolved from the flood histograms for the two detectors with two reflector arrangements. 80% of the events can be correctly assigned to each half. The detectors provide a two layer depth encoding capability. The photopeak value and average energy resolution of the first and second half of the crystal are almost the same. The average crystal energy resolutions of the  $4 \times 4$  and  $6 \times 6$  LYSO arrays with two reflector arrangements are 10.4% and 11.6%, respectively. The timing resolutions of the two detectors are 284 ps and 442 ps for an energy window of 400–600 keV. However, each quarter of the crystals cannot be clearly resolved for the two detectors with four reflector arrangements and further optimization is still required. The detectors developed in this work simultaneously provide a two layer depth encoding capability, good energy and timing resolution, and show great promise for developing high performance dedicated brain, whole body and total body PET scanners in the future.

## 1. Introduction

Positron emission tomography (PET) is an important tool in the early detection of many major diseases and biomedical research [1–4]. PET detectors commonly use a scintillator crystal array consisting of long crystals with a small cross section that is read out by photodetectors. Due to the uncertainty on the depth of interaction (DOI) of the incident gamma ray within the crystal, the spatial resolution of the PET scanner is deteriorated. The DOI effect is especially big for scanners with small detector ring diameter such as small animal and dedicated brain PET scanners, and scanners with a large axial field of view such as total body clinical PET scanners. In recent years, developing of depth encoding PET detectors has become a key research area in PET instrumentation [5,6]. Depth encoding PET detectors developed so far include dual-ended readout detector using two photodetectors coupled at both ends of a crystal array [7–9], phoswich detectors consisting of several layers of scintillator arrays

with different scintillation decay time [10–12], multiple-layered detectors individually read out by thin avalanche photodiodes (APDs) [13] or silicon photomultipliers (SiPMs) [14], single-ended readout detectors with depth dependent light distribution on photodetectors [15–19], detectors with wavelength discrimination [20], detectors with phosphor coated scintillator [21,22], monolithic scintillator detectors [23–26], semi-monolithic scintillator detectors [27,28], and other types of detectors [29,30]. Small animal, dedicated breast, and brain PET scanners using depth encoding detectors were also developed [11,14,31,32].

Depth encoding PET detectors consisting of two or four-layers of crystal arrays with different inter-crystal reflector arrangements in each layer were extensively studied [33–36] and used in dedicated breast [32] and brain PET scanners [37], and a PET scanner for ion range verification in heavy ion therapy [38]. More recently, the same four-layer DOI PET detector was also developed using crystal arrays made by subsurface laser engraving technique [39]. For PET detectors

\* Corresponding author.

E-mail address: [yf.yang@siat.ac.cn](mailto:yf.yang@siat.ac.cn) (Y. Yang).

**Table 1**

Detailed information about the four LYSO arrays measured in this work.

Array No.	No. of reflector arrangements	Crystal No.	Crystal size (mm <sup>3</sup> )
1	2	4 × 4	3 × 3 × 20
2	2	6 × 6	2 × 2 × 20
3	4	4 × 4	3 × 3 × 20
4	4	6 × 6	2 × 2 × 20

used in dedicated brain, whole body and total body PET scanners, in addition to a good DOI resolution, a good timing resolution is also required to reduce the uncertainty of the annihilation point on the measured line of response so as to increase the signal-to-noise ratio of the images [40,41], and a good energy resolution is required to efficiently reject the scattering events so as to improve the quantitation accuracy of the PET studies. In this work, a similar depth encoding PET detector technique that uses different inter-crystal reflector arrangements along the depths of a single layer crystal array is proposed. The detectors proposed in this work are expected to provide better energy and timing resolution since the interfaces between the crystal layers in the previous detectors no longer exist. Detectors using both two and four reflector arrangements along the crystal depths were fabricated and their performance was measured in this work.

## 2. Materials and methods

### 2.1. Concept of the depth encoding detectors

Fig. 1 shows schematic views of one detector unit consisting of 2 × 2 crystals of the two and four reflector arrangement detectors. The crystals are left uncut and only the inter-crystal reflector arrangements change along the crystal's depth. The four rectangle crystal faces are unpolished and the two small square crystal faces are polished. Both the enhanced specular reflector (ESR) of 65 μm thickness (3M, St. Paul, MN, USA) and optical glue (KE441-T, Shin-Etsu Chemical Co., Ltd, Japan) are used in between the crystals. The optical glue enhances the scintillation photon cross talk among crystals, while the ESR prevents it. When the crystal array is coupled to a position sensitive photodetector such as a SiPM array, the center of gravity of the distribution of scintillation photons on the photodetector produced in an interaction is depth dependent. The DOI can be measured by the flood histogram calculated by the center of gravity method. Fig. 1 also shows the expected patterns of the flood histograms of the detectors.

### 2.2. The 4 × 4 and 6 × 6 crystal arrays

Fig. 2 shows the structure of the four LYSO arrays measured in this work that consist of four or nine detector units of 2 × 2 crystals as shown in Fig. 1. Detailed information about the four LYSO arrays is shown in Table 1. All five outside faces of the arrays are wrapped with Teflon tape except the readout face that is coupled to the SiPM array with XIAMETER PMX-200 silicone oil (Dow Corning Corp, USA). The photodetector is a Hamamatsu S12642-0404PA-50 4 × 4 SiPM array (Hamamatsu Photonics, Japan). Each SiPM pixel is 3 × 3 mm<sup>2</sup> and the gap between the pixels is 0.2 mm. The total area of the SiPM array is 12.6 × 12.6 mm<sup>2</sup>. The schematic of the row and column summing readout circuit of the SiPM array is shown in Fig. 3. The 16 pixels of the SiPM array are read out by row and column summing circuit first and then the four row and four column signals are summed by using different weights as shown in Fig. 3 to generate four position encoding energy signals ( $X_1$ ,  $X_2$  and  $Y_1$ ,  $Y_2$ ) that are used to calculate the energy and flood histograms of the detectors.

### 2.3. Experimental setup

The photo and schematic of the experimental setup and the schematic of the electronics system are shown in Fig. 4. The experimental setup was placed in a large light tight box for light shielding. The four LYSO arrays were measured in both singles and coincidence modes. When a detector was measured in singles mode, the entire LYSO crystal array was uniformly irradiated by a 0.25 mm diameter <sup>22</sup>Na point source from one side with a distance of 60 mm. When a detector was measured in coincidence mode, a specific depth of the LYSO array was selectively irradiated by electric collimation using a 40 × 20 × 1.0 mm<sup>3</sup> LYSO slab detector coupling to a Hamamatsu R9800 PMT and the same <sup>22</sup>Na point source that were mounted on a translational table. The distances from the point source to the front of the collimation detector and the LYSO array are 35 mm and 60 mm, respectively. Four depths of 2.5 mm, 7.5 mm, 12.5 mm, and 17.5 mm from one end of the crystal arrays were measured. The four position-encoding energy signals from the SiPM array were digitized and stored as list mode data.

The timing resolution of the detector modules was measured by using a LYSO cylinder with a diameter of 20 mm and a length of 10 mm coupled to a Hamamatsu R13449 PMT as the reference detector. The reference detector was placed on the top of the detector module. The distances from the point source to the front of the reference detector and the LYSO array are 35 mm and 85 mm, respectively. Constant fraction discriminator was used for timing pick-off. The timing difference between the reference detector and the LYSO array detector was measured by a time-to-amplitude converter, and was then digitized and stored in the list mode data together with the four position encoding energy signals of the LYSO array detector and one energy signal of the reference detector. The timing resolution of the two identical reference detectors were also measured.

### 2.4. Data analysis

The energy of the detectors are calculated using the following equation:

$$E = X_1 + X_2 + Y_1 + Y_2 \quad (1)$$

where  $X_1$ ,  $X_2$ ,  $Y_1$  and  $Y_2$  are the four position-encoding energy signals from the SiPM array. The  $x$  and  $y$  coordinates of the flood histograms of the detectors are calculated using the following equation:

$$x = X_1 / (X_1 + X_2), y = Y_1 / (Y_1 + Y_2) \quad (2)$$

For data analysis, a preliminary flood histogram was first calculated using all the events acquired in singles mode. Crystal look up tables (LUTs) for either the entire crystal or specific depths of the crystals of an array could be created using the flood histogram. The data was re-analyzed by applying the crystal LUT to obtain the energy spectra of individual crystals. Then the photopeak value and full width at half maximum (FWHM) energy resolution were calculated by Gaussian fitting of the photopeak of the energy spectra. The flood histograms of the detectors can be recalculated by applying a crystal based energy window. The depth encoding capability of the detectors was evaluated by using the measured flood histograms.

To quantitatively estimate the depth decoding accuracy, the data measured at the four depths of 2.5 mm, 7.5 mm, 12.5 mm, and 17.5 mm were analyzed as the following. First, the flood histogram was projected along the blue dashed line as shown in Fig. 5 (left) for each crystal. Second, for detectors 1 and 2 that are with two reflector arrangements, the projection curves of the flood histograms measured at the first half (2.5 mm and 7.5 mm) and second half (12.5 mm and 17.5 mm) were obtained. For detectors 1–3, the projection curves of the flood histograms measured at four depths of 2.5 mm, 7.5 mm, 12.5 mm, and 17.5 mm were also obtained. The maximum value of the projection curves were normalized to 1. Vertical lines as shown in Fig. 5 (right)

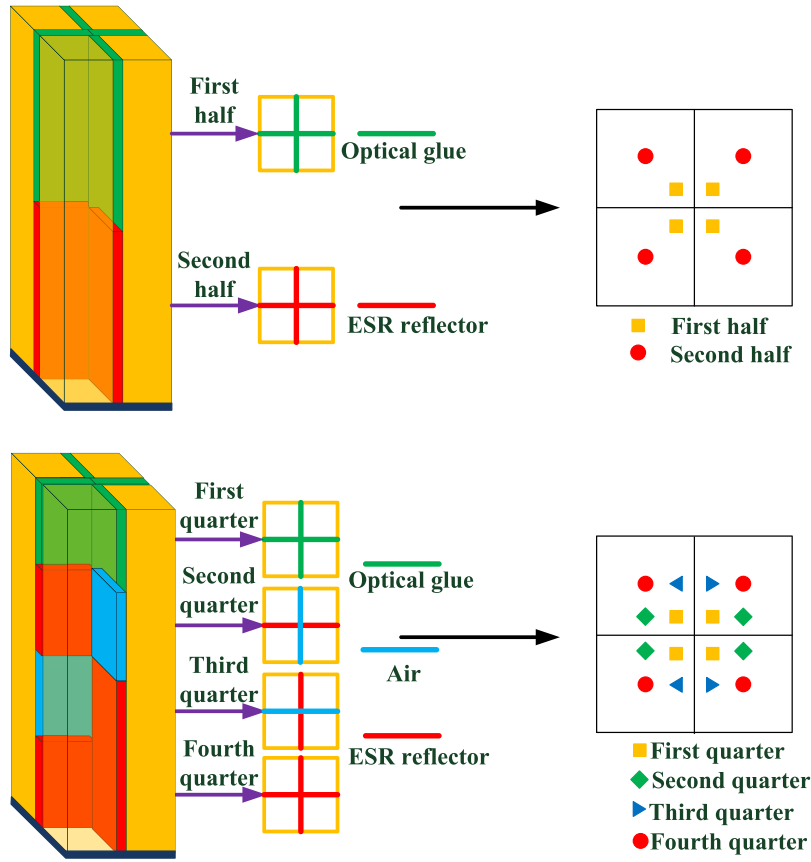


Fig. 1. Schematic views of the two (Top) and four (Bottom) reflector arrangement detectors and their expected flood histograms. The crystals are left uncut and only the reflector arrangements change along the crystal's depth.

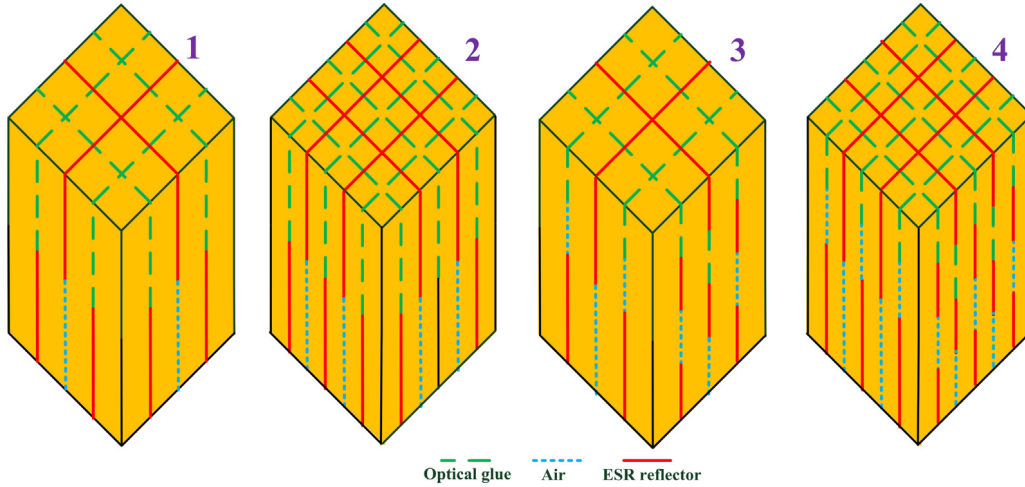


Fig. 2. The structures of the four LYSO arrays.

were drawn at the cross point of the projection curves. Third, as shown in Fig. 5 (right top) the events that fall in the left of the vertical line were assigned to the first half and those in the right were assigned to the second half of the crystal. As shown in Fig. 5 (right bottom), the events that fall in the left of the first vertical line were assigned to the first quarter, and those in between the first and the second vertical lines were assigned to the second quarter, and those in between the second and the third vertical lines were assigned to the third quarter, and those in the right of the third vertical lines were assigned to the fourth quarter. Finally the probabilities to make the correct assignment to each half or each quarter of the crystal were calculated. For detector

4, the data were not analyzed since some crystals cannot be clearly resolved.

The timing spectrum is the histogram of the timing difference between the reference detector and the LYSO array detector, or two reference detectors. The timing spectra of the entire detector and individual crystals of the detector were obtained by applying the crystal based energy window. The timing spectra were fitted with a Gaussian function. The FWHM timing resolutions of the two identical reference detectors, the reference detector and entire detector modules (each individual crystal of the detector module) were obtained. The timing resolution of two identical detector modules was obtained by the

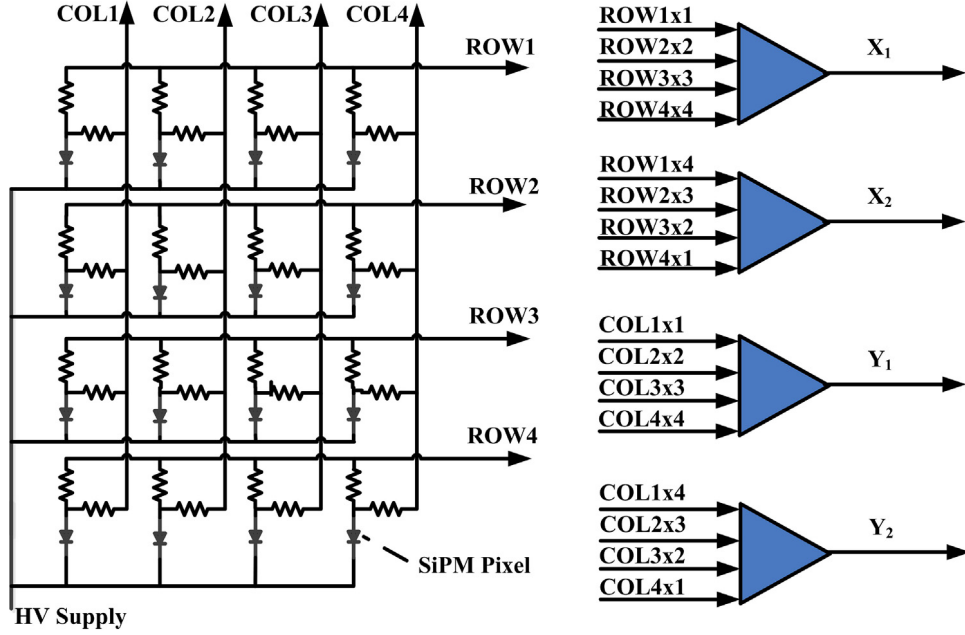


Fig. 3. Schematic of the row and column summing readout circuit of the SiPM array.

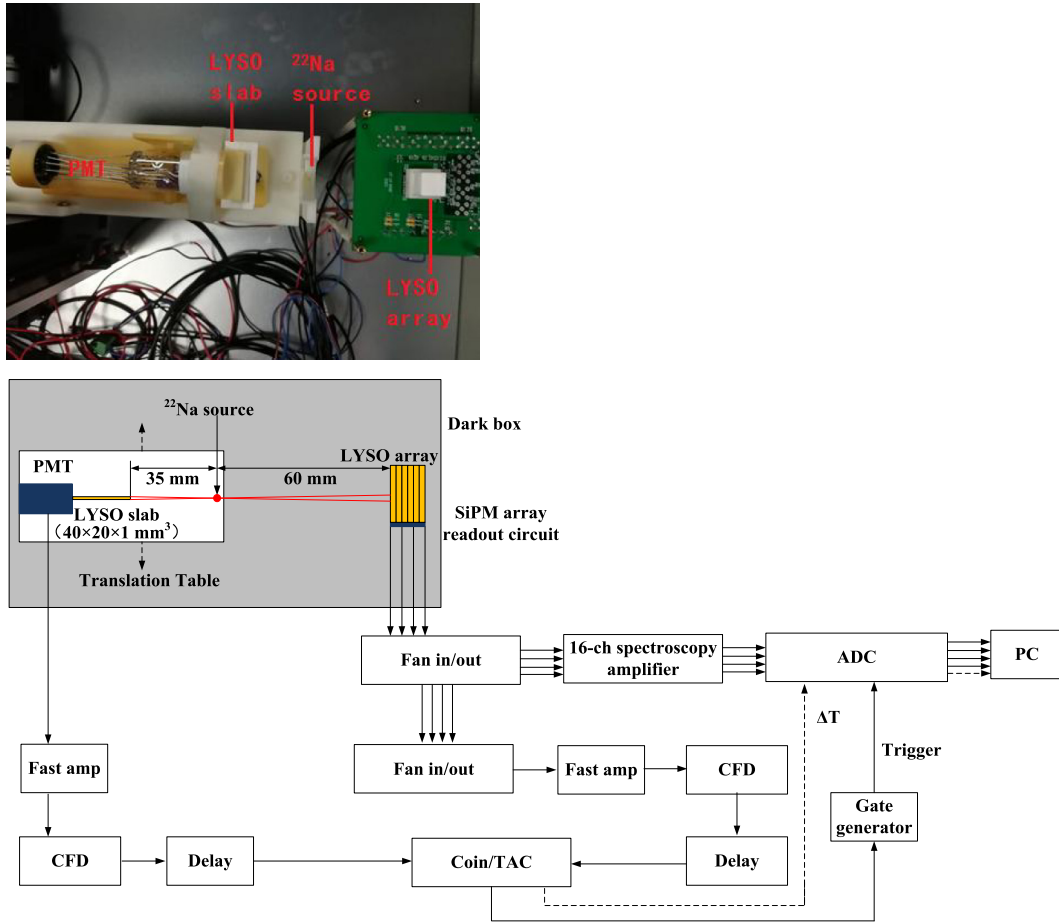


Fig. 4. (Top) Photo of the experimental setup, (bottom) schematics of experimental setup and the electronics system.

following equation:

$$\Delta T = \sqrt{(\Delta T_m^2 - \frac{\Delta T_r^2}{2}) \times 2}$$

(3)

$\Delta T_m$  is the timing resolution of the reference detector and detector module.  $\Delta T_r$  is the timing resolution of two identical reference detectors.

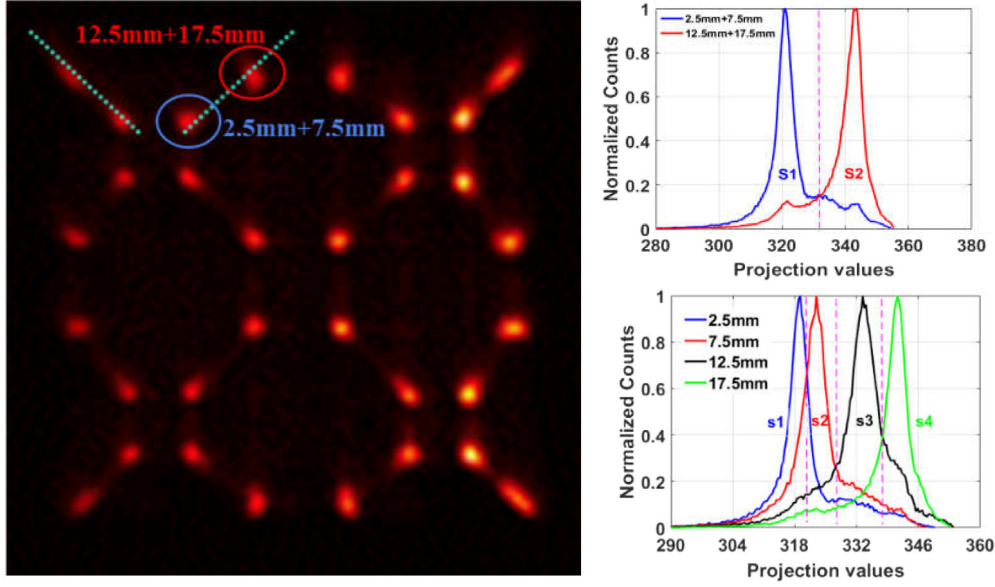


Fig. 5. (Left) A schematic showing how the flood histogram of each crystal measured at four depths was projected along a line. (top right) Projection curves of the first half and second half of one crystal, events were assigned to each half using the vertical line. (bottom right) Projection curves of the four quarters of one crystal, events were assigned to each quarter using the three vertical lines.

Table 2

The probabilities to make the correct assignment to each half of the crystals for detectors 1 and 2.

Detector No.	First half (%) (2.5 mm+7.5 mm)	Second half (%) (12.5 mm+17.5 mm)	Average of the entire crystal (%)
1	80.9 $\pm$ 4.5	81.2 $\pm$ 4.2	81.0 $\pm$ 2.3
2	80.7 $\pm$ 5.9	79.1 $\pm$ 7.5	79.9 $\pm$ 4.0

Table 3

The probabilities to make the correct assignment to each quarter of the crystals for detectors 1 to 3.

Detector No.	2.5 mm (%)	7.5 mm (%)	12.5 mm (%)	17.5 mm (%)	Average (%)
1	47.6 $\pm$ 11.1	46.9 $\pm$ 12.0	59.5 $\pm$ 5.8	52.3 $\pm$ 8.9	51.6 $\pm$ 4.6
2	51.5 $\pm$ 11.7	53.7 $\pm$ 12.8	52.8 $\pm$ 8.7	42.4 $\pm$ 11.1	50.1 $\pm$ 6.7
3	70.4 $\pm$ 6.0	47.6 $\pm$ 13.7	44.4 $\pm$ 15.6	61.9 $\pm$ 6.9	56.1 $\pm$ 7.4

### 3. Results

#### 3.1. Flood histograms measured at singles mode

The flood histograms of the four detectors measured at singles mode for all events and events with an energy window of 400 to 600 keV are shown in Figs. 6–9. For detectors 1 and 2 that have two reflector arrangements, all detector units, all crystals, and the first half and second half of the crystals are clearly resolved from the measured flood histograms. For detector 3 that has four reflector arrangements and 3 mm crystal size, all detector units and all crystals are clearly resolved, but each quarter of the crystals cannot be clearly resolved from the measured flood histograms. For detector 4 that has four reflector arrangements and 2 mm crystal size, all detector units can be resolved, but some crystals and each quarter of the crystals cannot be clearly resolved from the measured flood histograms.

#### 3.2. Flood histograms measured at four different depths

The flood histograms of all four detectors measured at the four depths of 17.5 mm, 12.5 mm, 7.5 mm, 2.5 mm, and the summed flood histograms of all four depths are shown in Figs. 10–13. For all four detectors, all crystals can be resolved from the flood histograms measured at one specific depth. For the two detectors with two reflector arrangements, the first half and the second half of the crystals can be clearly resolved from the summed flood histograms. The flood

histograms measured at different depths of each half (2.5 mm and 7.5 mm, 12.5 mm and 17.5 mm) show little difference. No further depth encoding capability can be provided within each half for the two detectors. Detectors 1 and 2 provide a two-layer depth encoding capability. For the two detectors with four reflector arrangements, the flood histograms change with depths, but each quarter of the crystals cannot be clearly resolved.

#### 3.3. Depth encoding accuracy

The projection curves measured at four depths of 2.5 mm, 7.5 mm, 12.5 mm, and 17.5 mm for one crystal of the four detectors are shown in Fig. 14. The probabilities to make the correct assignment to each half of the crystals for detectors 1 and 2 are shown in Table 2. The probabilities to make the correct assignment to each quarter of the crystals for detectors 1 to 3 are shown in Table 3. For detectors 1 and 2 that have two reflector arrangements, the projection curves of each half are clearly separated. ~80% of the events can be correctly assigned to each half. Most of the events that cannot be correctly assigned are probably inter-crystal scattering events. But the two projection curves within the same half almost overlap. For detectors 3 and 4 that have four reflector arrangements, the separation of the two projection curves within the same half is highly improved. On average, 56.1% of the events can be correctly assigned to each quarter for detector 3.



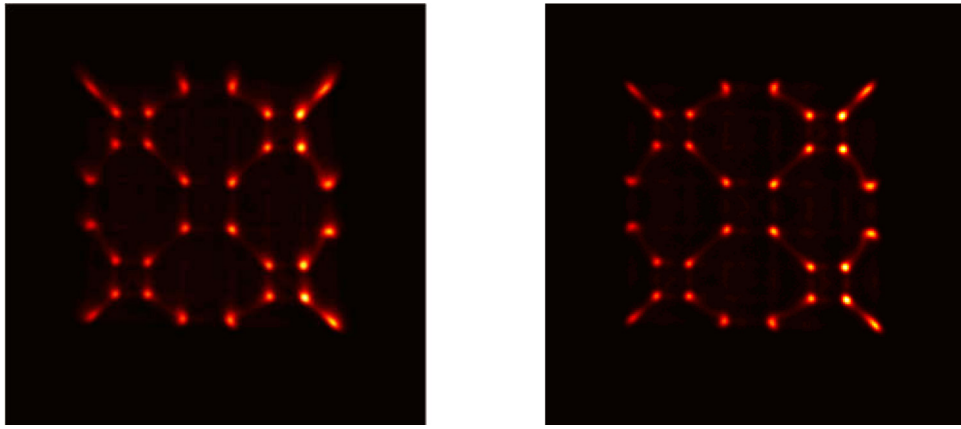


Fig. 6. Flood histograms of the  $4 \times 4$  LYSO arrays with two reflector arrangements measured in singles mode for (left) all events and (right) events with an energy window of 400 to 600 keV.

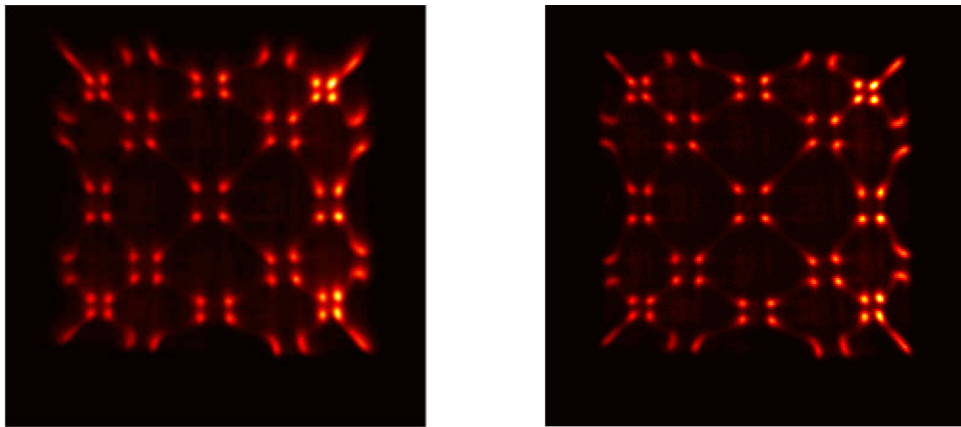


Fig. 7. Flood histograms of the  $6 \times 6$  LYSO arrays with two reflector arrangements measured in singles mode for (left) all events and (right) events with an energy window of 400 to 600 keV.

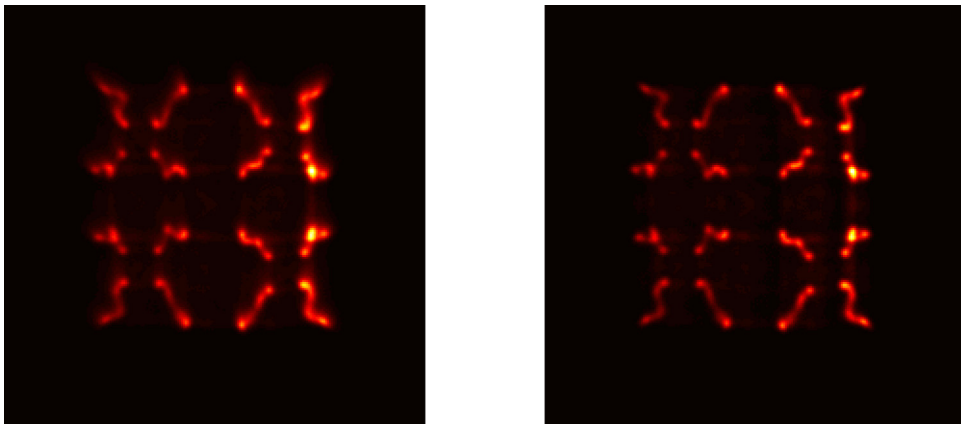


Fig. 8. Flood histograms of the  $4 \times 4$  LYSO arrays with four reflector arrangements measured in singles mode for (left) all events and (right) events with an energy window of 400 to 600 keV.

### 3.4. Energy resolution

The energy spectra of the entire array (all crystals), one entire crystal, and the first half and second half of one crystal are shown in Figs. 15 and 16 for singles-mode measurements with detectors 1 and 2, respectively. The average photopeak value and energy resolution results of the two detectors are shown in Table 4. The photopeak values of the first half and second half of the crystals are similar. The energy resolutions of the first half, second half, and entire crystals are all good.

The average energy resolutions of the entire crystals are 10.4% and 11.6% for detectors 1 and 2, respectively. The energy resolution results of detectors 3 and 4 are not further studied since each quarter of the crystals cannot be clearly resolved from the flood histograms.

### 3.5. Timing resolution

Fig. 17 shows the timing spectra for detectors 1 and 2. All timing resolution results are obtained with an energy window of 400~600 keV

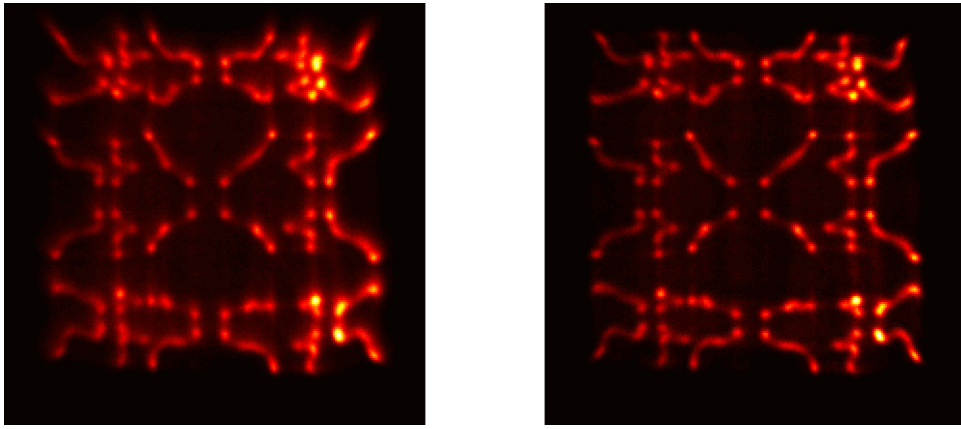


Fig. 9. Flood histograms of  $6 \times 6$  LYSO arrays with four reflector arrangements measured in singles mode for (left) all events and (right) events with an energy window of 400 to 600 keV.

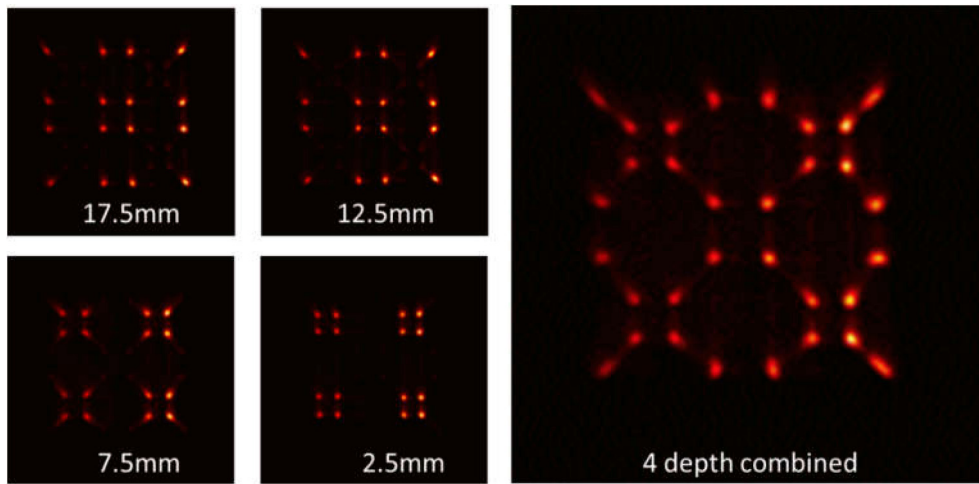


Fig. 10. Flood histograms of detector 1 measured at depths of 17.5 mm, 12.5 mm, 7.5 mm, 2.5 mm, and the summed flood histogram of all 4 depths for all events.

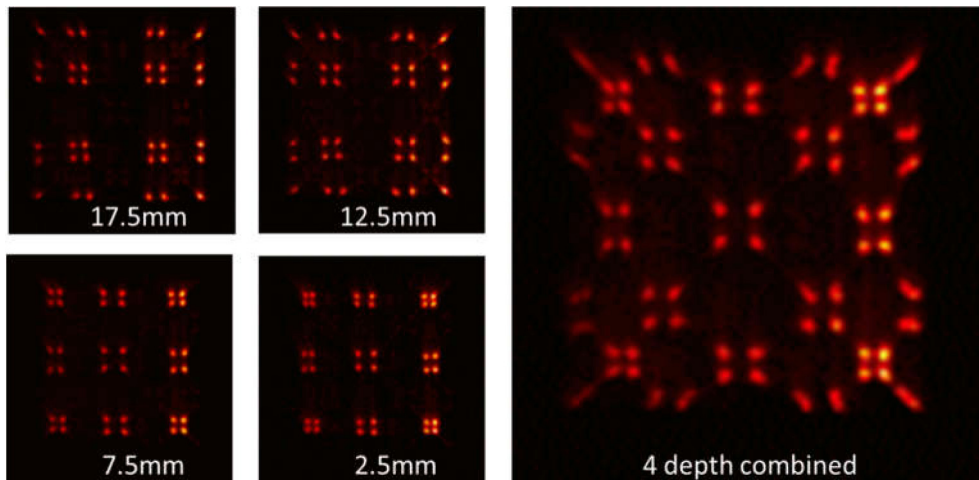


Fig. 11. Flood histograms of detector 2 measured at depths of 17.5 mm, 12.5 mm, 7.5 mm, 2.5 mm, and the summed flood histogram of all 4 depths for all events.

for both the reference detector and the two test detector modules. The FWHM timing resolutions of the entire detector are 357 ps and 430 ps for detectors 1 and 2, respectively. The average timing resolutions of individual crystals are  $357 \pm 9$  ps and  $415 \pm 17$  ps for detectors 1 and 2, respectively. The timing resolution of two identical reference

detectors is 417 ps. The timing resolutions of two identical detector 1 and detector 2 are 284 ps and 442 ps. The timing resolution of detector 1 is much better probably because the crystal and SiPM are one-to-one coupling.

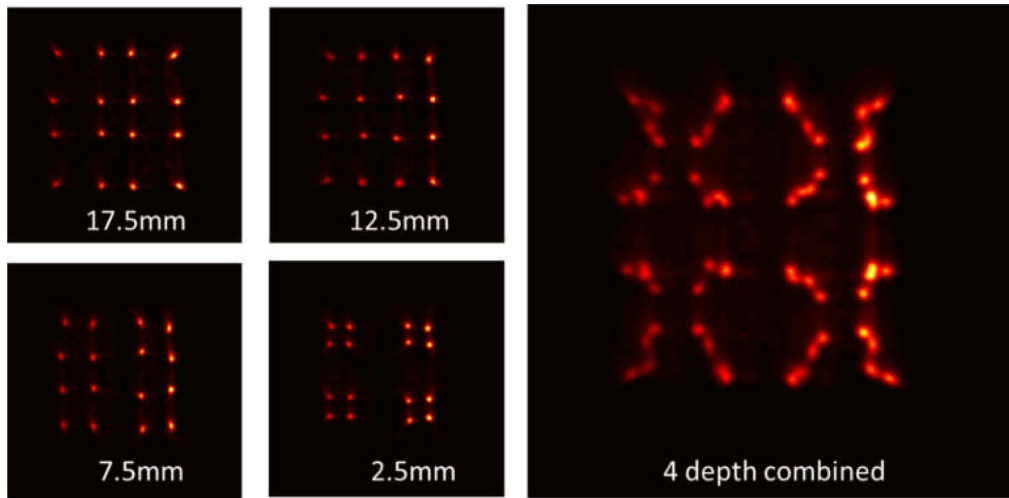


Fig. 12. Flood histograms of detector 3 measured at depths of 17.5 mm, 12.5 mm, 7.5 mm, 2.5 mm, and the summed flood histogram of all 4 depths for all events.

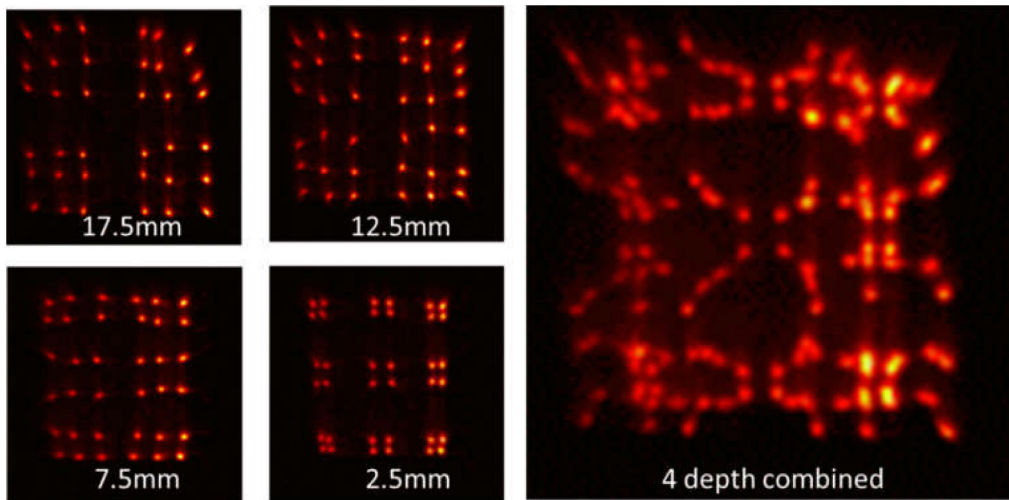


Fig. 13. Flood histograms of detector 4 measured at depths of 17.5 mm, 12.5 mm, 7.5 mm, 2.5 mm, and the summed flood histogram of all 4 depths for all events.

Table 4

The photopeak value and average energy resolution (%) of detectors 1 and 2.

Detector no.	First half		Second half		Entire crystal	
	Photopeak value	Average energy resolution (%)	Photopeak value	Average energy resolution (%)	Photopeak value	Average energy resolution (%)
1	$7.25 \pm 0.13$	$10.00 \pm 0.13$	$7.22 \pm 0.22$	$10.20 \pm 0.17$	$7.24 \pm 0.17$	$10.40 \pm 0.39$
2	$6.47 \pm 0.16$	$11.30 \pm 0.23$	$6.56 \pm 0.20$	$11.30 \pm 0.31$	$6.51 \pm 0.17$	$11.60 \pm 0.38$

#### 4. Discussions and conclusions

Depth encoding PET detectors using single layer crystal arrays with different inter-crystal reflector arrangements along the depth were manufactured and their performance was measured. For the two detectors with two reflector arrangements, the first and second half of the crystals can be clearly resolved from the flood histograms. 80% of the events can be correctly assigned to each half. The detectors provided a two layer depth encoding capability. For the two detectors with four reflector arrangements, each quarter of the crystals cannot be clearly resolved. It seems that the depth encoding capability of the detectors proposed in this work is not as good as previous detectors consisting of four layer crystal arrays with different reflector arrangements in each layer [33]. The main reason is that for the second and third quarters of the crystals, the scintillation photon cross talk is too large so the corresponding positions on the flood histograms move toward

the center of the detector unit. The reflector arrangements still need to be further optimized in order to resolve each quarter of the crystals. Since the spot size of each quarter of the crystal in the flood histogram is small, it is possible to resolve each quarter of the crystal by further optimizing the reflector arrangements. In the future, detectors with smaller crystal size and two reflector arrangements will be studied to further improve the spatial resolution of the detectors. Detectors with three reflector arrangements will also be studied.

The photopeak values of the first and second half of the crystals are similar for the two detectors with two reflector arrangements. The detectors achieved an energy resolution as good as 10.4%, which is close to the best energy resolution that can be achieved for an LYSO based PET detector and is much better than that obtained for the previous detectors consisting of four layer crystal arrays. For the previous detectors, crystal layer dependent energy resolutions of 15%–25% and 15%–18% were obtained when position sensitive photomultiplier tube [42] and digital SiPMs [43] are used, respectively. The detectors



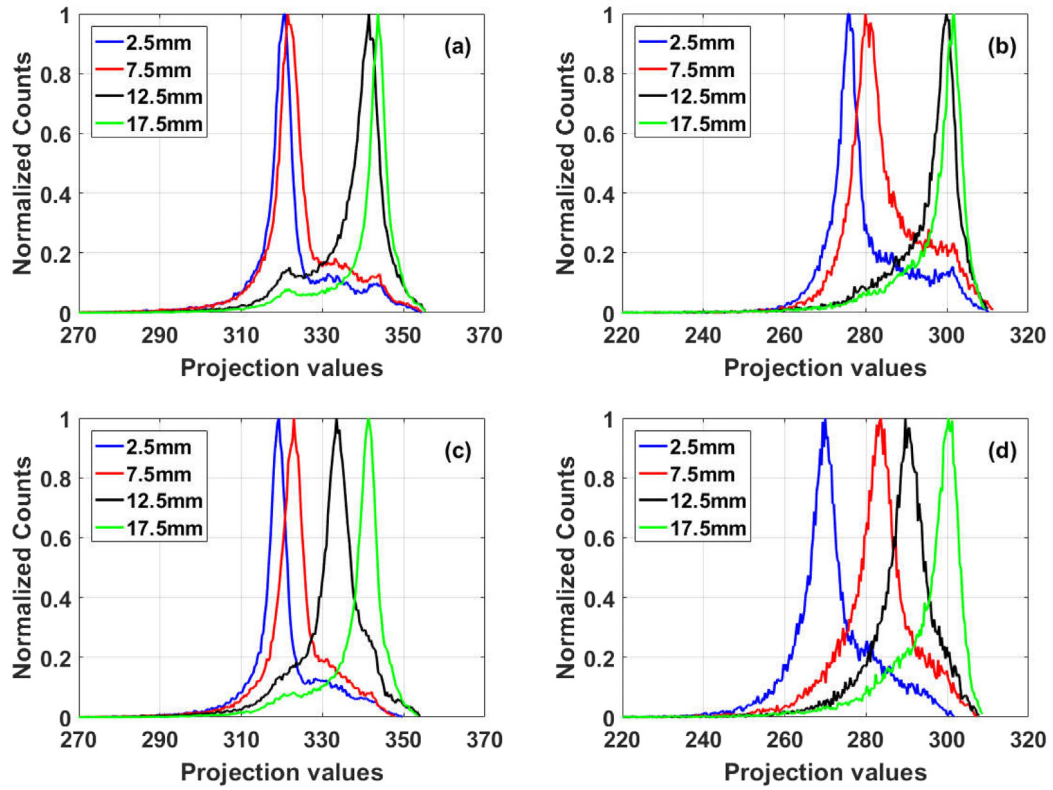


Fig. 14. Projection curves measured at four depths for one crystal of the four detectors, (a) detector 1, (b) detector 2, (c) detector 3, and (d) detector 4.

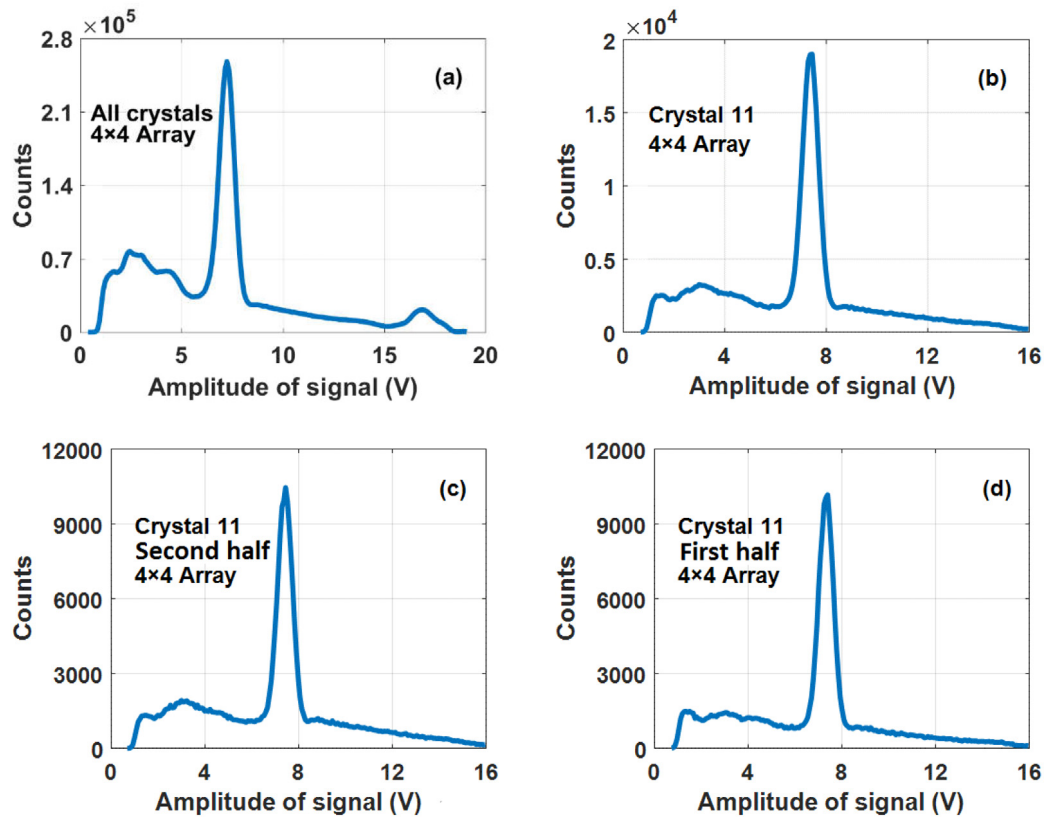


Fig. 15. Energy spectra of (a) all crystals, (b) crystal 11, (c) second half of crystal 11 and (d) first half of crystal 11 for detector 1.

achieved FWHM timing resolutions of 284 ps for 3 mm crystal and one-to-one crystal and SiPM coupling, and 442 ps for 2 mm crystals,

which is not as good as the state of art timing resolution of LYSO and SiPM based PET detectors as well as the previous detectors consisting

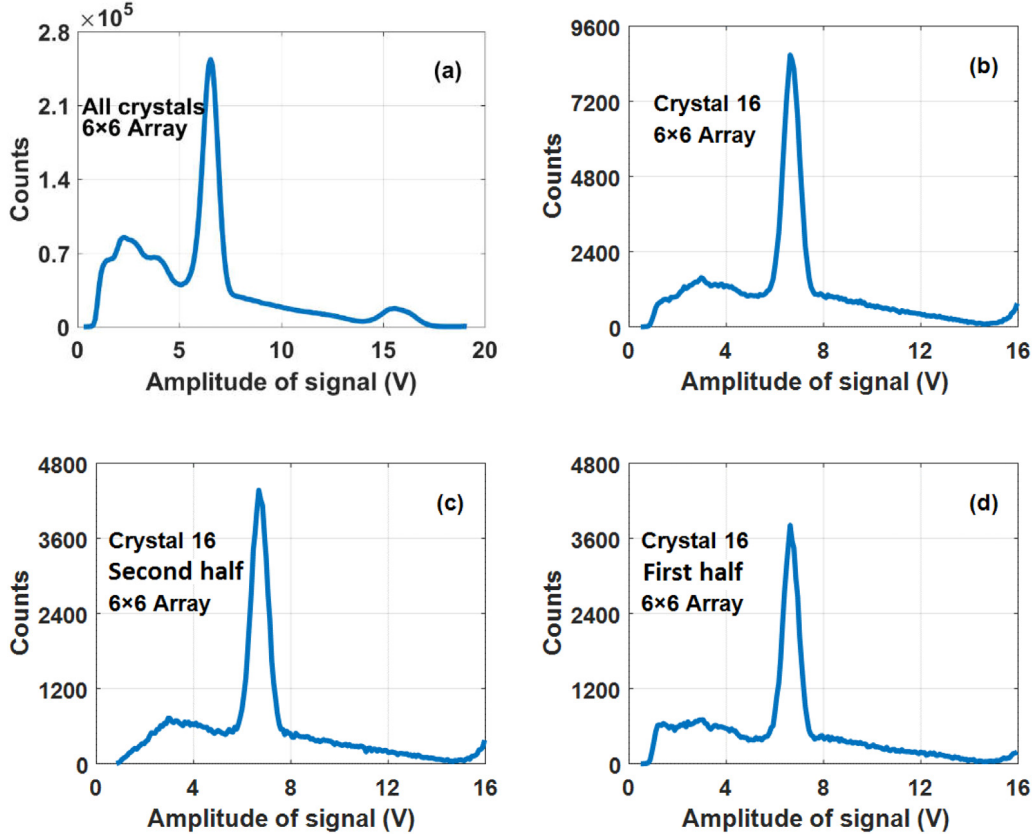


Fig. 16. Energy spectra of (a) all crystals, (b) crystal 16, (c) second half for crystal 16 and (d) first half for crystal 16 for detector 2.

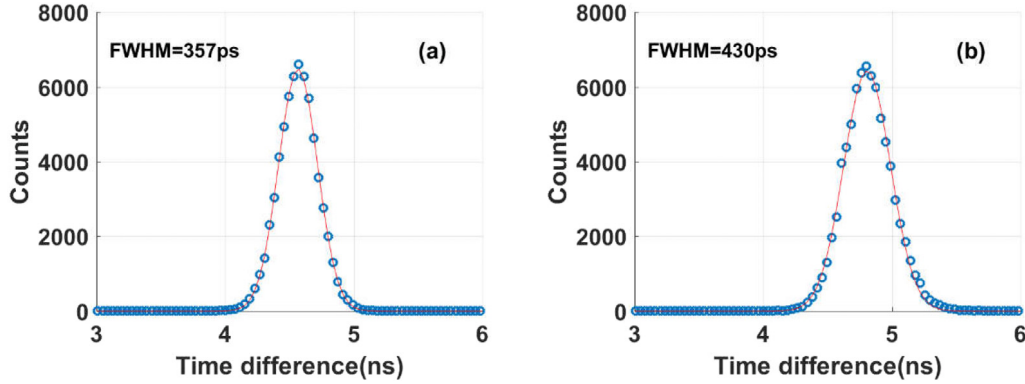


Fig. 17. Timing spectra of detectors (a) 1 and (b) 2 obtained with an energy window of 400~600 keV.

of four layer crystal arrays. The previous detectors achieved a timing resolution of  $\sim 270$  ps with digital SiPM readout [43]. In this work, the SiPM array was read out by a row and column summing readout and a constant fraction discriminator was used for the timing pick-off. The timing resolution can be further improved by using individually readout of the SiPM signals and a better timing pick-off method.

Other single-ended readout PET detectors were also developed to achieve depth encoding capability and high timing resolution simultaneously. A PET detector was developed by placing a thin light guide on the front of a scintillator array with unpolished crystals and the DOI was measured with depth dependent light distribution on photodetector [19]. The detector achieved a continuous DOI resolution of 4.1 mm, an energy resolution of 12.7%, and a timing resolution of 353 ps. The detector needs to use individual SiPM signal readout to calculate the DOI information and use unpolished crystals to achieve good DOI resolution, which may degrade the energy and timing resolution as

compared to detector using polished crystals. A PET detector was also developed by using phosphor coated crystal array with unpolished crystals and the DOI was measured by using the depth dependent signal decay time [21]. The detector achieved a DOI resolution of  $\sim 6.7$  mm, an energy resolution of 13.2%, and a timing resolution of 210 ps by using SiPM with high photon detection efficiency. Phosphor coating slightly degraded the timing and energy resolution of the detector, and a more complicated signal processing electronics was required to analyze the pulse shape so as to obtain the DOI information. The detectors developed in this work used polished crystals, multiplexed SiPM signal readout, and cheap signal processing electronics. The detectors of this work potentially can provide better timing and energy resolution but limited DOI resolution of 2 to 4 layers.

In conclusion, a novel depth encoding PET detector technology was proposed and evaluated in this work. The detectors developed in this work provided a two layer depth encoding capability, and are possible

to provide three to four layer depth encoding capability with more optimizations in the future. The detectors also provide good energy and timing resolution, and can be used to develop high performance dedicated brain, and whole body and total body PET scanners.

## Acknowledgments

This work is supported by the Peacock Innovation Team of Shenzhen, China (KQTD2016053117113327), the Basic Research Program of Shenzhen, China (JCYJ20160608153434110), the National Natural Science Foundation of China (81527804), the Hundred-Talent Program of the Chinese Academy of Sciences (Yongfeng Yang) and the Scientific Instrument Innovation Team of Chinese Academy of Sciences (GJJSTD20180002).

## References

- [1] S.R. Cherry, The 2006 Henry N. Wagner lecture: of mice and men (and positrons)—Advances in PET imaging technology, *J. Nucl. Med.* 47 (11) (2006) 1735–1745.
- [2] G. Muehlethner, J.S. Karp, Positron emission tomography, *Phys. Med. Biol.* 51 (13) (2006) R117–R137.
- [3] D.W. Townsend, Positron emission tomography/computed tomography, *Semin. Nucl. Med.* 38 (3) (2008) 152–166.
- [4] T. Jones, D.W. Townsend, History and future technical innovation in positron emission tomography, *J. Med. Imaging* 4 (1) (2017) 011013.
- [5] E. Berg, S.R. Cherry, Innovations in instrumentation for positron emission tomography, *Semin. Nucl. Med.* 48 (4) (2018) 311–331.
- [6] M. Ito, S.J. Hong, J.S. Lee, Positron emission tomography (PET) detectors with depth-of-interaction (DOI) capability, *Biomed. Eng. Lett.* 1 (2) (2011) 70–81.
- [7] W.W. Moses, S.E. Derenzo, Design studies for a PET detector module using a PIN photodiode to measure depth of interaction, *IEEE Trans. Nucl. Sci.* 41 (4) (1994) 1441–1445.
- [8] Y. Yang, P.A. Dokhale, R.W. Silverman, K.S. Shah, M.A. McClish, R. Farrell, G. Entine, S.R. Cherry, Depth of interaction resolution measurements for a high resolution PET detector using position sensitive avalanche photodiodes, *Phys. Med. Biol.* 51 (9) (2006) 2131–2142.
- [9] Y. Shao, R. Yao, T. Ma, A novel method to calibrate DOI function of a PET detector with a dual-ended-scintillator readout, *Med. Phys.* 35 (12) (2008) 5829–5840.
- [10] L. Eriksson, K. Wienhard, M. Eriksson, M.E. Casey, C. Knoess, T. Bruckbauer, J. Hamill, M. Schmand, T. Gremillion, M. Lenox, M. Conti, B. Bendriem, W.D. Heiss, R. Nutt, The ECAT HRRT: NEMA NEC evaluation of the HRRT system, the new high-resolution research tomograph, *IEEE Trans. Nucl. Sci.* 49 (5) (2002) 2085–2088.
- [11] Y. Wang, J. Seidel, B.M.W. Tsui, J.J. Vaquero, M.G. Pomper, Performance evaluation of the GE healthcare explore VISTA dual-ring small-animal PET scanner, *J. Nucl. Med.* 47 (11) (2006) 1891–1900.
- [12] S. Yamamoto, A dual layer DOI gso block detector for a small animal PET, *Nucl. Instrum. Methods Phys. Res. A* 598 (2) (2009) 480–484.
- [13] C.S. Levin, Design of a high-resolution and high-sensitivity scintillation crystal array for PET with nearly complete light collection, *IEEE Trans. Nucl. Sci.* 49 (5) (2002) 2236–2243.
- [14] M. Watanabe, A. Saito, T. Isobe, K. Ote, R. Yamada, T. Moriya, T. Omura, Performance evaluation of a high-resolution brain PET scanner using four-layer MPPC DOI detectors, *Phys. Med. Biol.* 62 (17) (2017) 7148–7166.
- [15] Y. Yang, Y. Wu, S.R. Cherry, Investigation of depth of interaction encoding for a pixelated LSO array with a single multi-channel PMT, *IEEE Trans. Nucl. Sci.* 56 (5) (2009) 2594–2599.
- [16] M. Ito, M.S. Lee, J.S. Lee, Continuous depth-of-interaction measurement in a single-layer pixelated crystal array using a single-ended readout, *Phys. Med. Biol.* 58 (5) (2013) 1269–1282.
- [17] H. Uchida, T. Sakai, H. Yamauchi, K. Hakamata, K. Shimizu, T. Yamashita, A novel single-ended readout depth-of-interaction PET detector fabricated using sub-surface laser engraving, *Phys. Med. Biol.* 61 (18) (2016) 6635–6650.
- [18] J.W. Son, M.S. Lee, J.S. Lee, A depth-of-interaction PET detector using a stair-shaped reflector arrangement and a single-ended scintillation light readout, *Phys. Med. Biol.* 62 (2) (2017) 465–483.
- [19] M. Pizzichemi, G. Stringhini, T. Niknejad, Z. Liu, P. Lecoq, S. Tavernier, J. Varela, M. Paganoni, E. Auffray, A new method for depth of interaction determination in PET detectors, *Phys. Med. Biol.* 61 (12) (2016) 4679–4698.
- [20] K. Shimazoe, A. Choghadi, H. Takahashi, K. Watanabe, Single side readout depth of interaction method with wavelength discrimination, *IEEE Trans. Nucl. Sci.* 63 (2) (2016) 679–684.
- [21] S.I. Kwon, A. Ferri, A. Gola, E. Berg, C. Piemonte, S.R. Cherry, E. Roncali, Reaching 200-ps timing resolution in a time-of-flight and depth-of-interaction positron emission tomography detector using phosphor-coated crystals and high-density silicon photomultipliers, *J. Nucl. Med.* 3 (4) (2016) 7.
- [22] H. Du, Y. Yang, J. Glodo, Y. Wu, K. Shah, S.R. Cherry, Continuous depth-of-interaction encoding using phosphor-coated scintillators, *Phys. Med. Biol.* 54 (6) (2009) 1757–1771.
- [23] C.W. Lerche, J.M. Benloch, F. Sanchez, N. Pavon, B. Escat, E.N. Gimenez, M. Fernandez, I. Torres, M. Gimenez, A. Sebastia, J. Martinez, Depth of gamma-ray interaction within continuous crystals from the width of its scintillation light-distribution, *IEEE Trans. Nucl. Sci.* 52 (3) (2005) 560–572.
- [24] S. Tavernier, P. Bruyndonckx, S. Leonard, O. Devroede, A high-resolution PET detector based on continuous scintillators, *Nucl. Instrum. Methods Phys. Res. A* 537 (1–2) (2005) 321–325.
- [25] T. Ling, T.K. Lewellen, R.S. Miyaoka, Depth of interaction decoding of a continuous crystal detector module, *Phys. Med. Biol.* 52 (8) (2007) 2213–2228.
- [26] S. Espana, R. Marcinkowski, V. Keereman, S. Vandenberghe, R. Van Holen, DigiPET: sub-millimeter spatial resolution small-animal PET imaging using thin monolithic scintillators, *Phys. Med. Biol.* 59 (13) (2014) 3405–3420.
- [27] Y.H. Chung, S.J. Lee, C.H. Baek, Y. Choi, New design of a quasi-monolithic detector module with DOI capability for small animal pet, *Nucl. Instrum. Methods Phys. Res. A* 593 (3) (2008) 588–591.
- [28] X. Zhang, X. Wang, N. Ren, Z. Kuang, X. Deng, X. Fu, S. Wu, Z. Sang, Z. Hu, D. Liang, X. Liu, H. Zheng, Y. Yang, Performance of a SiPM based semi-monolithic scintillator PET detector, *Phys. Med. Biol.* 62 (19) (2017) 7889–7904.
- [29] A.L. Goertzen, G. Stortz, J.D. Thiessen, D. Bishop, M.S. Khan, P. Kozlowski, F. Retière, G. Schellenberg, E. Shams, V. Sossi, C.J. Thompson, First results from a high-resolution small animal SiPM PET insert for PET/MR imaging at 7T, *IEEE Trans. Nucl. Sci.* 63 (5) (2016) 2424–2433.
- [30] S.J. Lee, C.H. Baek, Y.H. Chung, Y. Choi, W. Lee, A cross-stack quasi-monolithic detector with DOI capability for a small animal PET, in: 2008 IEEE Nuclear Science Symposium Conference Record, Dresden, Germany, 2008, pp. 3805–3809.
- [31] M. Balcerzyk, G. Kontaxakis, M. Delgado, L. Garcia-Garcia, C. Correcher, A.J. Gonzalez, A. Gonzalez, J.L. Rubio, J.M. Benloch, M.A. Pozo, Initial performance evaluation of a high resolution Albira small animal positron emission tomography scanner with monolithic crystals and depth-of-interaction encoding from a user's perspective, *Meas. Sci. Technol.* 20 (10) (2009) 104011.
- [32] M. Iima, Y. Nakamoto, S. Kanao, T. Sugie, T. Ueno, M. Kawada, Y. Mikami, M. Toi, K. Togashi, Clinical performance of 2 dedicated PET scanners for breast imaging: Initial evaluation, *J. Nucl. Med.* 53 (10) (2012) 1534–1542.
- [33] T. Tsuda, H. Murayama, K. Kitamura, T. Yamaya, E. Yoshida, T. Omura, H. Kawai, N. Inadama, N. Orita, A four-layer depth of interaction detector block for small animal PET, *IEEE Trans. Nucl. Sci.* 51 (5) (2004) 2537–2542.
- [34] N. Inadama, H. Murayama, M. Hamamoto, T. Tsuda, Y. Ono, T. Yamaya, E. Yoshida, K. Shibuya, F. Nishikido, 8-layer DOI encoding of 3-dimensional crystal array, *IEEE Trans. Nucl. Sci.* 53 (5) (2006) 2523–2528.
- [35] N. Inadama, H. Murayama, T. Yamaya, K. Kitamura, T. Yamashita, H. Kawai, T. Tsuda, M. Sato, Y. Ono, M. Hamamoto, Preliminary evaluation of four-layer BGO DOI-detector for PET, *IEEE Trans. Nucl. Sci.* 53 (1) (2006) 30–34.
- [36] F. Nishikido, N. Inadama, I. Oda, K. Shibuya, E. Yoshida, T. Yamaya, K. Kitamura, H. Murayama, Four-layer depth-of-interaction PET detector for high resolution PET using a multi-pixel S8550 avalanche photodiode, *Nucl. Instrum. Methods Phys. Res. A* 621 (1–3) (2010) 570–575.
- [37] T. Yamaya, E. Yoshida, T. Obi, H. Ito, K. Yoshikawa, H. Murayama, First human brain imaging by the jPET-D4 prototype with a pre-computed system matrix, *IEEE Trans. Nucl. Sci.* 55 (5) (2008) 2482–2492.
- [38] H. Tashima, E. Yoshida, N. Inadama, F. Nishikido, Y. Nakajima, H. Wakizaka, T. Shinaji, M. Nitta, S. Kinouchi, M. Suga, H. Haneishi, T. Inaniwa, T. Yamaya, Development of a small single-ring OpenPET prototype with a novel transformable architecture, *Phys. Med. Biol.* 61 (4) (2016) 1795–1809.
- [39] A. Mohammadi, N. Inadama, E. Yoshida, F. Nishikido, K. Shimizu, T. Yamaya, Improvement of crystal identification performance for a four-layer DOI detector composed of crystals segmented by laser processing, *Nucl. Instrum. Methods Phys. Res. A* 866 (2017) 29–35.
- [40] E. Berg, E. Roncali, M. Kapusta, J. Du, S.R. Cherry, A combined time-of-flight and depth-of-interaction detector for total-body positron emission tomography, *Med. Phys.* 43 (2) (2016) 939–950.
- [41] J.P. Schmoll, J.S. Karp, M. Werner, S. Surti, Parallax error in long-axial field-of-view PET scanners—a simulation study, *Phys. Med. Biol.* 61 (14) (2016) 5443–5455.
- [42] E. Yoshida, K. Kitamura, T. Tsuda, K. Shibuya, T. Yamaya, N. Inadama, T. Hasegawa, H. Murayama, Energy spectra analysis of the four-layer DOI detector for the brain PET scanner: jPET-D4, *Nucl. Instrum. Methods Phys. Res. A* 557 (2) (2006) 664–669.
- [43] E. Yoshida, I. Somlai-Schweiger, H. Tashima, S.I. Ziegler, T. Yamaya, Parameter optimization of a digital photon counter coupled to a four-layered DOI crystal block with light sharing, *IEEE Trans. Nucl. Sci.* 62 (3) (2015) 748–755.